

Observation of superconductivity in a nontrivial \mathcal{Z}_2 approximant quasicrystal

Pavan Kumar Meena ^{*,1} Rahul Verma ^{*,2} Arushi,¹ Sonika Jangid,¹ Roshan Kumar Kushwaha,¹ Rhea Stewart,³ Adrian D. Hillier,³ Bahadur Singh ^{†,2} and Ravi Prakash Singh ^{† 1}

¹*Department of Physics, Indian Institute of Science*

Education and Research Bhopal, Bhopal, 462066, India

²*Department of Condensed Matter Physics and Materials Science,*

Tata Institute of Fundamental Research, Mumbai 400005, India

³*ISIS Facility, STFC Rutherford Appleton Laboratory,*

Harwell Science and Innovation Campus, Oxfordshire, OX11 0QX, UK

arXiv:2501.00554v1 [cond-mat.supr-con] 31 Dec 2024

*These authors contributed equally to this work.

†Corresponding emails: bahadur.singh@tifr.res.in, rpsingh@iiserb.ac.in

ABSTRACT

Superconductivity and nontrivial topology are highly sought-after phenomena in quantum materials. While many topological crystalline materials have been found to exhibit superconductivity, their presence in quasicrystals - materials with a unique aperiodic yet ordered structure - has remained largely unexplored. In this work, we report the discovery of superconductivity in a monoclinic approximant to the decagonal quasicrystal $\text{Al}_{13}\text{Os}_4$, that exhibits a high superconducting transition temperature and a nontrivial electronic structure. The resistivity, magnetization, specific heat, and μSR measurements confirm superconductivity with a critical temperature of ~ 5.47 K. Detailed electronic structure and symmetry analysis reveal nontrivial state with $\mathcal{Z}_2 = 1$ and spin-polarized conducting surface states. Importantly, we identify three-dimensional saddle point van Hove singularities with substantial flat energy dispersion at the Fermi level, which can enhance superconductivity. Our results highlight a rich interplay between superconductivity and nontrivial electronic states in $\text{Al}_{13}\text{Os}_4$, demonstrating it as a unique platform for exploring unconventional superconducting states in quasicrystalline materials.

INTRODUCTION

Quasicrystals (QCs), first discovered by Shechtman *et al.* in 1984, exhibit long-range atomic order without periodicity, thereby occupying a distinct structural regime between periodic and amorphous materials. This long-range order manifests in sharp Bragg peaks resulting from crystallographically forbidden rotational symmetries, such as 5-, 8-, 10-, and 12-fold symmetries. Initially identified in intermetallic alloys, QCs have since been observed in a variety of systems, though they remain less explored compared to periodic and amorphous materials [1]. QCs exhibit intriguing electronic and magnetic properties, including long-range magnetic order, low-temperature order-disorder transitions, pseudogaps near the Fermi level, and unconventional magnetic behavior [2–5].

Advances in theoretical explorations and experimental characterization have recently revealed diverse phenomena in QCs, such as non-trivial bulk and surface states, Fulde-Ferrell-Larkin-Ovchinnikov (FFLO) superconductivity, nematic order, and localized Cooper pair distributions [6–11]. However, these phenomena challenge conventional solid-state theories, such as Bloch's theorem and topological band theory, which rely on the translational symmetry, and

the Bardeen-Cooper-Schrieffer (BCS) theory of superconductivity, which assumes Cooper pair formation with zero center-of-mass momentum [12]. QCs are often accompanied by a periodic phase resulting from their projection along rational directions, known as approximants. These approximants, while periodic with ordered motifs and symmetries, share local similarities with QCs and serve as a bridge between periodic and aperiodic structures. This periodic framework helps simplify the understanding of the complex properties of QCs [13, 14]. For instance, superconductivity has been observed in QCs, such as a Bergmann-type Al-Mn-Zn alloy with a transition temperature (T_C) around 0.05 K [15], and a van der Waals-layered two-dimensional (2D) dodecagonal QC with a T_C of 1 K [16, 17] as well as in their approximants. Such studies infer that superconductivity remains robust under variations of the atomic arrangement from periodic to quasiperiodic, though the superconducting T_C in QCs remains relatively low.

Meanwhile, various theoretical studies have predicted topological phases and their candidate materials in QCs by exploiting the periodic symmetries of approximants or considering long-range quasicrystalline order as arising from periodic structures in higher-dimensional spaces [18–20]. Despite these predictions, no quasicrystalline materials have yet shown both high-temperature superconductivity and a nontrivial electronic structure. Notably, decagonal QCs and their approximants exhibit quasiperiodic ordering in the plane and periodicity along one axis. They can provide a particularly unique system for exploring superconductivity and nontrivial topological phenomena in materials that combine quasiperiodicity and periodicity [21]. However, the superconductivity or nontrivial topological structure in decagonal QCs remains elusive.

In this work, we report the discovery of superconductivity in the decagonal approximant $\text{Al}_{13}\text{Os}_4$ [22, 23], and demonstrate its nontrivial electronic structure. Through comprehensive experimental investigations, including magnetization, resistivity, specific heat, and advanced μSR measurements, we observe bulk superconductivity with a T_C of 5.47(2) K and preserved time reversal symmetry in superconducting ground state. Despite its complex structure, the superconducting properties exhibit good agreement with the weak coupling limit of the BCS theory. Our detailed bulk and surface state calculations reveal nontrivial Z_2 invariants and spin-polarized topological surface states that cross the Fermi level. We also identify 2D Fermi sheets and saddle-point van Hove singularities at the Fermi level, which may enhance superconducting T_C in $\text{Al}_{13}\text{Os}_4$. The combination of high T_C , bulk superconductivity, and nontrivial topological features makes $\text{Al}_{13}\text{Os}_4$ as a promising candidate for exploring topological superconductivity. Our work opens new avenues for studying QCs and their approximants as materials for unconventional superconductivity and topological phenomena in quantum condensed matter physics.

RESULTS

Crystal structure

The crystal structure of the approximant decagonal QCs $\text{Al}_{13}\text{Os}_4$ adopts a low-symmetry monoclinic structure with space group $C2/m$ (No. 12) and C_{2h} point-group symmetry (see Figs. 1(a)-(c)), isostructural to the Y phase of $\text{Al}_{13-x}(\text{Co}_{4(1-y)}\text{Ni}_{4y})$ or $\text{Al}_{11}\text{Co}_4$ [22, 23]. Fig. 1(d) shows the powder X-ray diffraction pattern (XRD) and Rietveld refinement (detailed structural parameters and Wyckoff positions given in the SM).

The structure comprises of two quasi-periodic layers stacking along the \vec{b} direction with a periodicity of $\sim 4 \text{ \AA}$. A quasiperiodic atomic layer in the $\vec{b} = 0$ plane connects to another layer at $\vec{b} = 1/2$ plane through a shift in the lattice constant by $a/2$ to form a periodic unit cell (Fig. 1(b)). It consists of slightly distorted pentagons and rhombi (Fig. 1(a)), with an Al atom occupying one vertex of the pentagon and Os atoms occupying the remaining vertices. Three Al atoms also lie in this Os-Al pentagon. Smaller Al pentagons, made up of five Al atoms with an Os atom at the center, also appear in the adjacent layers. Despite slight differences in Al and Os occupancy, the local structural configuration in the two quasi-periodic layers is nearly identical. In the periodic approximant phase, pentagonal elements are distorted, unlike the regular pentagons in the decagonal quasicrystal phase, representing the primary difference between the two phases [22, 24]. Figure 1(c) shows the repetitive arrangement of distorted pentagons and rhombi that tile in the plane to generate the periodic crystal structure. It is important to note that a decagonal QC with two quasiperiodic layers with a periodicity length of about 0.4 nm is the most anisotropic case, whereas other decagonal QCs have four, six, and eight layers in a periodic unit with periodicities of about 0.8 , 1.2 , and 1.6 nm , respectively, exhibiting progressively lower anisotropies.

Bulk superconductivity

Figure 1(e) presents the temperature-dependent electrical resistivity $\rho(T)$ of $\text{Al}_{13}\text{Os}_4$ under zero-applied magnetic field. A sharp decrease in $\rho(T)$ to zero at a transition temperature $T_C = 5.47(2) \text{ K}$ confirms the onset of superconductivity, the highest T_C observed to date in any known quasicrystals and approximants (see SM for details). The high-temperature behavior of $\rho(T)$ is metallic, which is well described by Wiesmann's parallel resistor model (black solid line in Fig. 1(e)). The residual resistivity ratio, $\rho(300)/\rho(10) = 7.5$, further corroborates the metallic nature of the system (additional details on fitting parameters, Kadowski-Woods ratio, and the Hall measurement data are given in SM).

Specific heat measurements reveal a lambda-shaped anomaly observed at $T_C = 5.44(2)\text{K}$, confirming bulk superconductivity consistent with resistivity and magnetization data (see SM). Fig. 1(f), shows temperature-dependent electronic specific heat, fitted with the BCS model. The fitting results yield a superconducting gap value ($\frac{\Delta(0)}{k_B T_C}$) of 1.72(1), indicating weak coupling BCS superconductivity in $\text{Al}_{13}\text{Os}_4$. Additionally, the density of states at the Fermi level $D(E_F)$ estimated to be 9.15(4) states eV^{-1} f.u. $^{-1}$, and the Debye temperature θ_D , 340(4) K, comparable to those found in elemental Os and Al, the approximant phase of quasicrystals, and other complex intermetallic compounds [13]. Using the McMillan model, the electron-phonon coupling strength λ_{e-ph} is estimated to be 0.63(1), indicating weakly coupled superconductivity in $\text{Al}_{13}\text{Os}_4$. A detailed mathematical description of this analysis is provided in the SM.

Figure 1(g) displays the temperature-dependent magnetization of $\text{Al}_{13}\text{Os}_4$ measured in a 1 mT applied field. Both the zero field-cooled warming (ZFCW) and the field-cooled cooling (FCC) curves exhibit a sharp diamagnetic response below $T_C = 5.45(6)$ K, confirming the Meissner effect and the onset of superconductivity. The observed difference between the ZFCW and FCC curves is attributed to flux pinning, a characteristic of type-II superconductors. The AC susceptibility and magnetization loop further confirm the superconducting transition and vortex pinning (see SM). Using M versus H and M versus T data and applying the Ginzburg-Landau (GL) relations (Figs. 1(h) and 1(i)) the lower and upper critical fields are determined to be obtained as $H_{C1} = 7.5(4)$ mT and $H_{C2} = 1.24$ (1) T, respectively. From these values, two important length scales are extracted, the penetration depth $\lambda_{GL}(0) = 249(5)$ nm and coherence length $\xi_{GL}(0) = 16.2(9)$ nm. The GL parameter $\kappa_{GL} = \lambda_{GL}(0)/\xi_{GL}(0) = 15.3(1)$ indicates strong type-II superconductivity. The thermodynamic critical field is obtained as $H_C = 58.3(8)$ mT. Moreover, the calculated Maki parameter $\alpha_M = 0.14$ suggests that the Pauli limiting effect has a negligible influence on superconductivity, with orbital limiting being the dominant factor.

μSR results

To further investigate the superconducting gap symmetry and ground-state properties of $\text{Al}_{13}\text{Os}_4$, we performed Muon spin rotation and relaxation (μSR) measurements at ISIS, RAL UK, employing both transverse field (TF) and longitudinal field (LF) geometries, as illustrated in Figs. 2(a) and 2(b).

TF- μSR and fully gapped superconductivity: TF- μSR experiments are used to examine the superconducting gap symmetry by measuring the magnetic penetration depth and field distribution in the mixed state. To establish a well-ordered flux line lattice (FLL), experiments

were performed under field-cooled conditions. Figure 2(c) shows the asymmetry spectra (precession signal) measured above and below T_C in an applied field of 30 mT, where the faster relaxation rate at 0.5 K compared 7 K reflects the inhomogeneous field distribution from the FLL. In all temperature ranges, time domain TF- μ SR asymmetry spectra are well described by the Gaussian-damped oscillatory function given as,

$$A(t) = A_1 \exp\left(-\frac{1}{2}\sigma^2 t^2\right) \cos(\gamma_\mu B_1 t + \phi) + A_2 \cos(\gamma_\mu B_2 t + \phi), \quad (1)$$

where A_1 and A_2 denote the initial asymmetries corresponding to the sample and non-relaxing background from the silver sample holder, B_1 and B_2 are the local magnetic fields sensed by the muons in the sample and sample holder, and $\gamma_\mu/2\pi = 135.5$ MHz/T is the muon gyromagnetic ratio. ϕ denotes the common phase offset. The Gaussian depolarization rate, σ , is given by $\sigma^2 = \sigma_N^2 + \sigma_{sc}^2$, where $\sigma_N = 0.219 \mu s^{-1}$ is the temperature-independent depolarization rate associated with the nuclear dipole moment and σ_{sc} represents the depolarization rate from the FLL. The temperature dependence σ_{sc} exhibits a plateau at low temperatures. Subsequently, it decreases as the temperature increases before finally reaching zero at T_C (Fig. 2(e)). To determine the superconducting gap, the temperature-dependent penetration depth $\lambda^{-2}(T) \propto \sigma_{sc}$ was fitted with an isotropic s -wave BCS superconductor in the clean limit [25],

$$\frac{\sigma_{sc}(T)}{\sigma_{sc}(0)} = \frac{\lambda^{-2}(T)}{\lambda^{-2}(0)} = 1 + 2 \int_{\Delta(T)}^{\infty} \left(\frac{\partial f}{\partial E}\right) \frac{E dE}{\sqrt{E^2 - \Delta(T)^2}}, \quad (2)$$

where $\lambda(0)$ is the London penetration depth, $f = [1 + e^{(E/k_B T)}]^{-1}$ is the Fermi distribution function, and $\Delta(T)$ is the BCS superconducting gap function given as $\Delta(T) = \Delta_0 \tanh[1.82(1.018((T_C/T) - 1))^{0.51}]$. Fitting of $\lambda^{-2}(T)$ with Eq. 2 provides a superconducting gap as $\Delta(0) = 0.79(3)$ meV. The normalized gap, $\Delta(0)/k_B T_C = 1.78(6)$, is consistent to that expected for a BCS weak coupling superconductor. To determine the penetration depth $\lambda^{\mu SR}(0)$, the following relation used where $k_{GL} \geq 5$ and $H \leq H_{C2}$ [26];

$$\sigma_{sc}(\mu s^{-1}) = 4.854 \times 10^4 (1 - h) [1 + 1.21(1 - \sqrt{h})^3] \lambda^{-2}, \quad (3)$$

with $h = H/H_{C2}(0)$ the reduced field. The calculated value of $\lambda^\mu(0) = 268.6(7)$ nm closely matches the values from the magnetization as well as those obtained through the analysis of the London penetration depth. Considering the measured residual resistance, we derive a ratio of the Faber-Pippard superconducting coherence length and the electronic transport mean free path (ξ_0/l_e) that approaches the clean limit of the superconductor [See SM for individual electronic parameter calculations] [26].

Uemura plot classified superconductors as conventional and unconventional based on the transition temperature T_C and Fermi temperature T_F . The T_C/T_F ratio is 0.002 ($T_C = 5.47(2)$ K, $T_F = 2038(9)$ K; see SM for calculation), marked by a blue square in Fig. 2(f) for $\text{Al}_{13}\text{Os}_4$, indicating its location close to the region of unconventional superconductors.

ZF- μ SR and preserved time-reversal symmetry: We further employ zero-field (ZF)- μ SR measurements to probe spontaneous magnetization linked to time-reversal symmetry breaking in the superconducting state. The overlapped ZF- μ SR asymmetry spectra below and above T_C (Fig. 2(d)) show no detectable spontaneous magnetization, confirming the preserved time-reversal symmetry in $\text{Al}_{13}\text{Os}_4$. The best description of the ZF spectra is given as,

$$A(t) = A_0 G_{KT}(t) \exp(-\Lambda t) + A_{bg}, \quad (4)$$

where A_0 is the initial sample asymmetry and A_{bg} is the non-decaying background from muons stopped in the silver sample holder. The Gaussian static Kubo-Toyabe (KT) function ($G_{KT}(t)$) is given as [27]:

$$G_{KT}(t) = \frac{1}{3} + \frac{2}{3}(1 - \Delta^2 t^2) \exp\left(-\frac{\Delta^2 t^2}{2}\right), \quad (5)$$

The relaxation parameter Δ is associated with randomly oriented, static local fields from nuclear moments, and the electronic relaxation rate, Λ , both remains nearly constant above and below the superconducting T_C , indicating preserved time-reversal symmetry in $\text{Al}_{13}\text{Os}_4$.

Electronic structure and topology

To examine the electronic topology of decagonal approximant $\text{Al}_{13}\text{Os}_4$, we performed first-principles calculations considering experimental parameters with $C2/m$ symmetry. The calculated band structure and density of states (DOS) exhibit metallic behavior, with several bands crossing the Fermi level E_f (Figs. 3(a)-(b)). The four bands, labeled $\gamma_{i=1-4}$, occupy the substantial area of the BZ at the Fermi level. Among these, the γ_2 and γ_3 bands display a 2D character with open Fermi sheets at E_f (Fig. 3(c)). In contrast, the γ_1 band exhibits 3D saddle-points energy dispersion with a large area flat band close to E_f as shown in Fig. 3(b). At the Γ point, the electron (blue) and hole (red) bands cross to form a saddle point with a slowly decaying quadratic dispersion along the $\Gamma - X$ direction. This saddle point gives van Hove singularities (vHSs) near the Fermi level. Such features in the electronic structure are expected to enhance superconducting instability, in agreement with the experimental observations.

Next, we calculate the Sommerfeld-specific heat coefficient and compare it with the experimental data. From the results, we obtain a total DOS at the Fermi level, $D(E_f) = 5.38$ states eV^{-1} f.u. $^{-1}$. This yields a theoretical Sommerfeld specific-heat coefficient $\gamma_0 = \frac{\pi^2 k_B^2}{3} D(E_f)$ of

12.70 mJ mol⁻¹ K⁻², which is $\sim 60\%$ of the experimentally measured value of $\gamma_n = 21.54(7)$ mJ mol⁻¹ K⁻². This difference infers that electron-mass renormalization due to saddle point could be larger than expected, potentially indicating strong correlation effects. Using the calculated (γ_0) and experimental (γ_n) specific-heat coefficients, we estimate the electron-phonon coupling constant (λ_{e-ph}) using the relation $\frac{\gamma_n}{\gamma_0} = (1 + \lambda_{e-ph})$. The calculated λ_{e-ph} is 0.69, which is in close agreement with the experimental value of 0.63(1).

Having discussed the electronic properties, we now explore the topological electronic state of Al₁₃Os₄ with spin-orbit coupling (SOC) (see Figs. 3(d)-(g)). The band structure without SOC shows several nodal crossings between different bands near the Fermi level (see SM). These crossings form nodal lines in the bulk BZ. However, due to the lower C_{2h} point-group symmetry and inversion symmetry in Al₁₃Os₄, the inclusion of SOC gaps out these nodal band crossings, resulting in a continuous bandgap at each k -point in the BZ. This local bandgap facilitates the calculations of the \mathcal{Z}_2 topological invariant similar to insulators [28]. In Fig. 3(d), we show the product of parity eigenvalues at various time-reversal invariant points for bands $\gamma_{i=1-3}$ [28]. This parity analysis reveals a nontrivial \mathcal{Z}_2 invariant when either γ_2 or γ_3 bands are considered as valence bands. Figures 3(f)-(g) display the (001) surface band structure and corresponding spin texture. Several spin-momentum-locked surface states are seen to cross the Fermi level. Specifically, within the bulk band-inverted region around +0.3 eV, a clear nontrivial Dirac cone surface state appears inside the projected bulk bands. The lower state of this Dirac cone exhibits substantial bandwidth and crosses the Fermi level. The calculated nonzero \mathcal{Z}_2 invariant and non-trivial Dirac cone surface states confirm that Al₁₃Os₄ is \mathcal{Z}_2 nontrivial. The presence of nontrivial spin-polarized surface states can become superconducting via the bulk proximity effect, leading to unconventional superconductivity in Al₁₃Os₄.

SUMMARY AND DISCUSSION

Our results position Al₁₃Os₄ as a distinctive decagonal QC approximant that exhibits high superconducting T_C and nontrivial electronic topology. It crystallizes in a monoclinic structure with $C2/m$ symmetry group, where two aperiodic layers are stacked along the \vec{b} direction to form a periodic unit cell. Analysis of resistivity, specific heat, magnetization and μ SR measurements demonstrates that Al₁₃Os₄ exhibits bulk type-II superconductivity with $T_C = 5.47(2)$ K, an upper critical field $H_{C2}(0) = 1.24(1)$ T. Zero-field electronic specific heat data align with weak-coupling BCS superconductivity, yielding a superconducting gap of 1.72(1), which closely matches the BCS-type superconductivity gap of 1.78(6) obtained with TF- μ SR measurements. Importantly, the time-reversal symmetry is preserved in the superconducting

state within the detection limit of the μ SR. The observed weak-coupling, clean-limit BCS superconductivity with preserved time-reversal symmetry in the superconducting ground state of $\text{Al}_{13}\text{Os}_4$ suggests phonon-mediated pairing despite the quasicrystalline atomic arrangement. Our first-principles calculations reveal that $\text{Al}_{13}\text{Os}_4$ is a topological metal with a nontrivial \mathcal{Z}_2 invariant and vHSs near the Fermi level.

The aperiodic crystal structure of QCs and their approximants induces both local and global breaks in translational symmetry, which makes a momentum-space perspective inadequate for understanding their properties. The possibility of irregular lattice vibrations arising from aperiodicity may result in unconventional non-BCS superconductivity [12]. However, the observation of weak-coupling superconductivity with preserved time-reversal symmetry in $\text{Al}_{13}\text{Os}_4$ raises important questions about the interplay between aperiodic structures and conventional superconductivity. QCs are also known to suppress superconducting T_C when transitioning from approximants to the QC phase. The higher T_C observed in $\text{Al}_{13}\text{Os}_4$ may thus be attributed to its 2D approximant nature, which retains periodicity in one direction. This contrasts with other 3D QCs such as i-Al-Zn-Mn [15] and the 2D quasicrystalline $\text{Ta}_{1.6}\text{Te}$ [16], where the superconductivity is more suppressed.

Moreover, the incorporation of heavy transition metal atoms in $\text{Al}_{13}\text{Os}_4$ enhances SOC strength, which plays a crucial role in the realization of non-trivial topological state with non-trivial \mathcal{Z}_2 , topological surface states and VHS in the energy spectrum. These features are analogous to recently discovered kagome superconductors such as AV_3Sb_5 ($A = \text{Cs, K}$) [29]. These results strengthen that $\text{Al}_{13}\text{Os}_4$ is a promising candidate for exploring topological superconductivity, potentially stabilizing Majorana modes within the vortex cores of its superconducting surface states, which are naturally proximitized by the bulk superconductivity. Note that materials exhibiting both topologically nontrivial surface states and intrinsic superconductivity are rare. Notable examples include $\text{FeSe}_{1-x}\text{Te}_x$ [30], doped Bi_2Se_3 [31], and $\text{Sn}_{1-x}\text{In}_x\text{Te}$ [32], all of which show promising signs of unconventional superconductivity. The combination of superconductivity and nontrivial electronic topology in $\text{Al}_{13}\text{Os}_4$ presents an exciting platform to explore the interplay between superconductivity, topological effects, and vHSs, and offers new insights into the possible realization of topological superconductivity in QCs and their approximants.

METHODS

Sample preparation and characterization— $\text{Al}_{13}\text{Os}_4$ was synthesized by arc melting high-purity Os (4N) and Al (4N) in the 13: 4 stoichiometric ratio. The arc melting process was carried out

on a water-cooled copper hearth under a high-purity Ar (4N) atmosphere. To ensure homogeneity, the alloy was re-melted multiple times after each flip. To examine phase purity and crystal structure characterization, room temperature powder X-ray diffraction was performed using a PANalytical X'pert Pro diffractometer using a monochromatic x-ray source with $\lambda = 1.5406 \text{ \AA}$ CuK $_{\alpha}$ radiation. VESTA visualization tool was used to visualize the crystal structure [33].

Superconducting and normal state characterization– To investigate the superconducting state, magnetization measurements as a function of temperature and magnetic field were performed using a Quantum Design Superconducting Quantum Interference Device (SQUID) magnetometer in vibrating sample magnetometer (VSM) mode. Electrical transport measurements were conducted using the four-probe technique on a Quantum Design Physical Property Measurement System (PPMS). Heat capacity measurements at zero magnetic field were carried out on the PPMS system using the two-tau relaxation method. A small piece of the sample was affixed to the sapphire holder of the calorimeter using Apiezon-N grease and cooled to 1.9 K. Measurements were then performed in heating mode. To obtain the heat capacity of the sample, the signals from the calorimeter and the grease, measured independently under identical conditions, were subtracted.

μ SR experiments– μ SR measurements were performed using the MuSR spectrometer at the ISIS pulsed muon facility, STFC RAL, U.K. μ SR is a microscopic technique for directly probing superconducting materials by measuring spontaneous magnetic fields and vortex state with high sensitivity. It can detect minute variations in internal magnetic fields as small as $\sim 1 \mu\text{T}$ (detection limit) and magnetic moments down to a few hundredths of a μ_B , through the precession of muons with the Larmor frequency $\nu_{\mu} = \gamma_{\mu}/(2\pi)B_{\mu}$ in local magnetic fields at the muon site. The Al $_{13}$ Os $_4$ system was studied in a zero field (ZF) to detect internal fields. Sample position achieves a near-zero field environment with a tolerance of $1 \mu\text{T}$, which is made possible by three sets of orthogonal coils and an active-field compensation system. Additionally, transverse field (TF) modes, employing a magnetic field perpendicular to the incident muon spin direction, were utilized to explore the gap of a superconductor. For measurement, 3g of powdered sample was mounted on a silver holder with diluted GE varnish and placed in a dilution refrigerator. Nearly 100 % spin-polarized positive muons were implanted, decaying into positrons and neutrinos after a mean lifetime of $2.2 \mu\text{s}$, and the decayed positrons were collected by four detector groups positioned around the sample position: top, bottom, forward, and backward. The asymmetry of the muon signal is determined using the relation $A(t) = [N_F(t) - \alpha N_B(t)]/[N_F(t) + \alpha N_B(t)]$, where $N_B(t)$ and $N_F(t)$ are the number of detector counts in the forward and backward positions and α is an experiment-specific constant determined from calibration measurements. The reference provides an in-depth explanation of the μ SR technique and detector geometries [34]. The experimental data was analyzed using MANTID software.

First-principles calculations– Electronic structure calculations were performed within the frame-

work of density functional theory based on the projected augmented wave (PAW) method using Vienna *ab-initio* simulation package [35, 36]. The generalized gradient approximation (GGA) [37] was used to include the exchange-correlation effects and the spin-orbit coupling was added self-consistently. The kinetic energy cut-off of 400 eV for the plane-wave basis set and a Γ -centered $11 \times 11 \times 13$ k mesh for Brillouin zone sampling were used. We used experimental lattice constants and relaxed the internal atomic positions until the residual forces on each ion were less than 10^{-2} eV \AA^{-1} . To explore the topological electronic state, we generated a material-specific tight-binding model Hamiltonian using the VASP2WANNIER90 interface [38]. We used Os s , d and Al s , p orbitals to generate the Wannier functions. The surface states and spin texture were obtained using the iterative Green's functions method [39, 40].

DATA AVAILABILITY

All data that support the findings of this study are available within the paper and/or Supplemental Materials. Additional data related to this paper may be requested from R.P.S. (rpsingh@iiserb.ac.in).

-
- [1] Shechtman, D., Blech, I., Gratias, D. & Cahn, J. W. Metallic phase with long-range orientational order and no translational symmetry. Phys. Rev. Lett. **53**, 1951 (1984).
 - [2] Deguchi, K. et al. Quantum critical state in a magnetic quasicrystal. Nat. Mater. **11**, 1013 (2012).
 - [3] Hafner, J. & Krajčí, M. Electronic structure and stability of quasicrystals: Quasiperiodic dispersion relations and pseudogaps. Phys. Rev. Lett. **68**, 2321 (1992).
 - [4] Nayak, J. et al. Bulk electronic structure of quasicrystals. Phys. Rev. Lett. **109**, 216403 (2012).
 - [5] Tamura, R. et al. Experimental observation of long-range magnetic order in icosahedral quasicrystals. J. Am. Chem. Soc. **143**, 19938 (2021).
 - [6] Chen, R., Chen, C.-Z., Gao, J.-H., Zhou, B. & Xu, D.-H. Higher-order topological insulators in quasicrystals. Phys. Rev. Lett. **124**, 036803 (2020).
 - [7] Fan, J. & Huang, H. Topological states in quasicrystals. Front. Phys. **17**, 13203 (2022).
 - [8] Ghadimi, R., Sugimoto, T., Tanaka, K. & Tohyama, T. Topological superconductivity in quasicrystals. Phys. Rev. B **104**, 144511 (2021).
 - [9] Sakai, S. & Arita, R. Exotic pairing state in quasicrystalline superconductors under a magnetic field. Phys. Rev. Research **1**, 022002 (2019).

- [10] Araújo, R. N. & Andrade, E. C. Conventional superconductivity in quasicrystals. Phys. Rev. B **100**, 014510 (2019).
- [11] Liu, Y.-B., Zhou, J. & Yang, F. Nematic superconductivity and its critical vestigial phases in the quasi-crystal. Phys. Rev. Lett. **133**, 136002 (2024).
- [12] Sakai, S., Takemori, N., Koga, A. & Arita, R. Superconductivity on a quasiperiodic lattice: Extended-to-localized crossover of cooper pairs. Phys. Rev. B **95**, 024509 (2017).
- [13] Graebner, J. E. & Chen, H. S. Specific heat of an icosahedral superconductor, $\text{Mg}_3\text{Zn}_3\text{Al}_2$. Phys. Rev. Lett. **58**, 1945 (1987).
- [14] Wagner, J. L., Biggs, B. D., Wong, K. M. & Poon, S. J. Specific-heat and transport properties of alloys exhibiting quasicrystalline and crystalline order. Phys. Rev. B **38**, 7436 (1988).
- [15] Kamiya, K. et al. Discovery of superconductivity in quasicrystal. Nat. Commun. **9**, 154 (2018).
- [16] Tokumoto, Y. et al. Superconductivity in a van der waals layered quasicrystal. Nat. Commun. **15**, 1529 (2024).
- [17] Terashima, T. et al. Anomalous upper critical field in the quasicrystal superconductor $\text{Ta}_{1.6}\text{Te}$. npj Quantum Materials **9**, 56 (2024).
- [18] Kraus, Y. E., Lahini, Y., Ringel, Z., Verbin, M. & Zilberberg, O. Topological states and adiabatic pumping in quasicrystals. Phys. Rev. Lett. **109**, 106402 (2012).
- [19] Kraus, Y. E. & Zilberberg, O. Topological equivalence between the fibonacci quasicrystal and the harper model. Phys. Rev. Lett. **109**, 116404 (2012).
- [20] Cain, J. D., Azizi, A., Conrad, M., Griffin, S. M. & Zettl, A. Layer-dependent topological phase in a two-dimensional quasicrystal and approximant. Proc. Natl. Acad. Sci. USA **117**, 26135 (2020).
- [21] Singh, B., Lin, H. & Bansil, A. Topology and symmetry in quantum materials. Advanced Materials **35**, 2201058 (2023).
- [22] Zhang, B., Gramlich, V. & Steurer, W. $\text{Al}_{13-x}(\text{Co}_{1-y}\text{Ni}_y)_4$, a new approximant of the decagonal quasicrystal in the Al-Co-Ni system. Z. Kristallogr **210**, 498 (1995).
- [23] Li, X. Z., Shi, N. C., Ma, Z. S., Ma, X. L. & Kuo, K. H. Structure of $\text{Al}_{11}\text{Co}_4$, a new monoclinic approximant of the Al-Co decagonal quasicrystal. Philos. Mag. Lett. **72**, 79 (1995).
- [24] Steurer, W., Haibach, T., Zhang, B., Kek, S. & Lück, R. The structure of decagonal $\text{Al}_{70}\text{Ni}_{15}\text{Co}_{15}$. Acta Cryst. **49**, 661 (1993).
- [25] Brandt, E. H. Properties of the ideal ginzburg-landau vortex lattice. Phys. Rev. B **68**, 054506 (2003).
- [26] Devarakonda, A. et al. Clean 2D superconductivity in a bulk van der waals superlattice. Science **370**, 231 (2020).

- [27] Hayano, R. S. *et al.* Zero-and low-field spin relaxation studied by positive muons. Phys. Rev. B **20**, 850 (1979).
- [28] Fu, L. & Kane, C. L. Topological insulators with inversion symmetry. Phys. Rev. B **76**, 045302 (2007).
- [29] Ortiz, B. R. *et al.* CsV₃Sb₅: A Z₂ topological kagome metal with a superconducting ground state. Phys. Rev. Lett. **125**, 247002 (2020).
- [30] Zhang, P. *et al.* Observation of topological superconductivity on the surface of an iron-based superconductor. Science **360**, 182 (2018).
- [31] Sasaki, S. *et al.* Topological superconductivity in Cu_xBi₂Se₃. Phys. Rev. Lett. **107**, 217001 (2011).
- [32] Sasaki, S. *et al.* Odd-parity pairing and topological superconductivity in a strongly spin-orbit coupled semiconductor. Phys. Rev. Lett. **109**, 217004 (2012).
- [33] Momma, K. & Izumi, F. VESTA 3 for three-dimensional visualization of crystal, volumetric and morphology data. J. Appl. Cryst. **44**, 1272 (2011).
- [34] Hillier, A. D. *et al.* Muon spin spectroscopy. Nat. Rev. Methods Primers **2**, 4 (2022).
- [35] Kohn, W. & Sham, L. J. Self-consistent equations including exchange and correlation effects. Phys. Rev. **140**, A1133 (1965).
- [36] Kresse, G. & Joubert, D. From ultrasoft pseudopotentials to the projector augmented-wave method. Phys. Rev. B **59**, 1758 (1999).
- [37] Perdew, J. P., Burke, K. & Ernzerhof, M. Generalized gradient approximation made simple. Phys. Rev. Lett. **77**, 3865 (1996).
- [38] Mostofi, A. A. *et al.* wannier90: A tool for obtaining maximally-localised wannier functions. Comput. Phys. Commun. **178**, 685 (2008).
- [39] Wu, Q., Zhang, S., Song, H.-F., Troyer, M. & Soluyanov, A. A. Wanniertools: An open-source software package for novel topological materials. Comput. Phys. Commun. **224**, 405 (2018).
- [40] Sancho, M. P. L., Sancho, J. M. L., Sancho, J. L. & Rubio, J. Highly convergent schemes for the calculation of bulk and surface green functions. J. Phys. F: Met. Phys. **15**, 851 (1985).

ACKNOWLEDGMENTS

P.K.M. acknowledges the funding agency Council of Scientific and Industrial Research (CSIR), Government of India, for providing the SRF fellowship (Award No: 09/1020(0174)/2019-EMR-I). R.P.S. acknowledges the Science and Engineering Research Board, Government of India, for the Core Research Grant No. CRG/2023/000817 and ISIS, STFC, UK, for providing

beamtime for the μ SR experiments. The work at TIFR Mumbai is supported by the Department of Atomic Energy of the Government of India under Project No. 12-R&D-TFR-5.10-0100 and benefited from the HPC resources of TIFR Mumbai.

AUTHOR CONTRIBUTIONS

RPS conceived the project. PKM, A, SJ, RKK, and RPS prepared the samples and conducted the characterization. RPS, ADH, RS, and PKM carried out the μ SR experiments and data analysis. RV and BS performed the first-principles calculations and symmetry analysis. PKM, A, RV, BS, and RPS wrote the manuscript, with input from all authors. This work is supervised by RPS (experiment) and BS (theory).

COMPETING INTERESTS

The authors declare no competing interests.

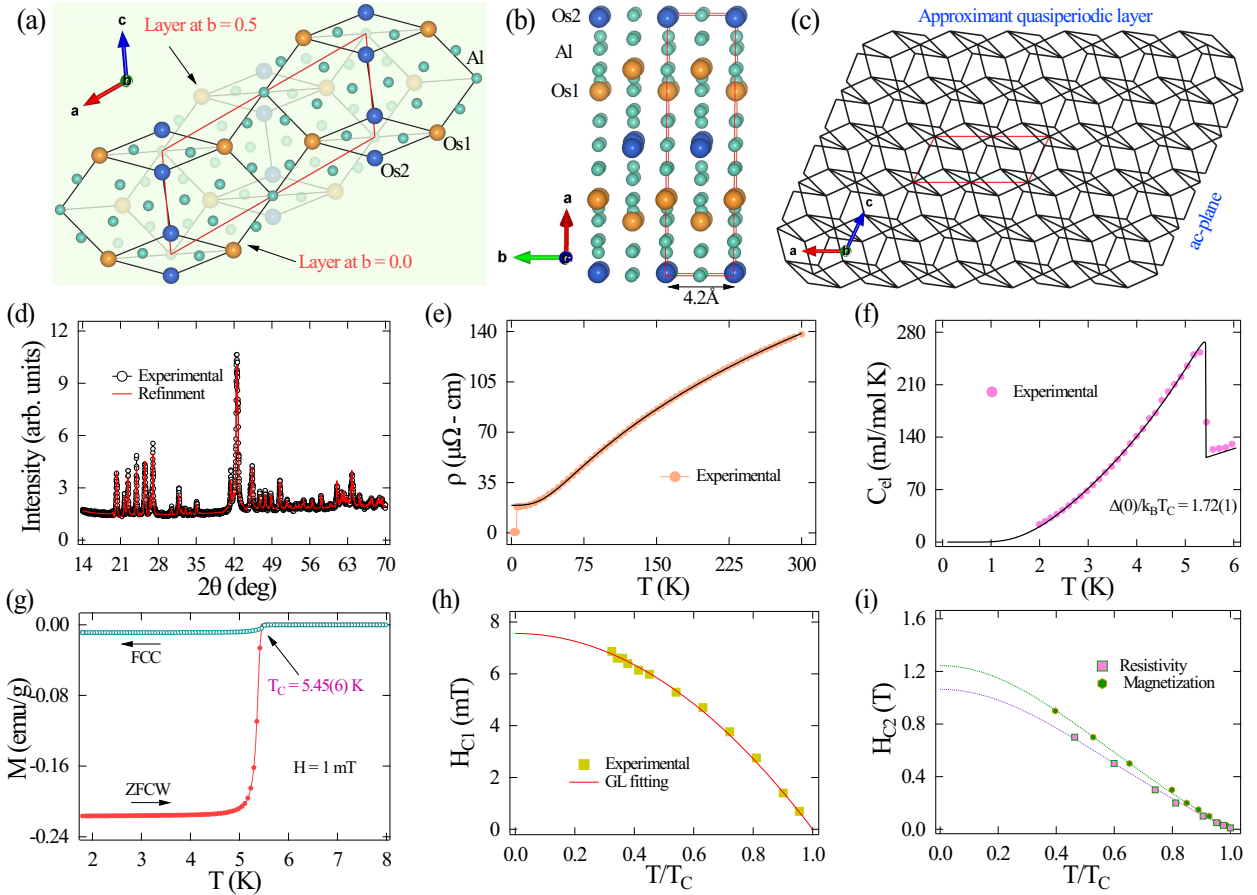


FIG. 1. **Crystal structure and bulk superconductivity characterization of the decagonal quasicrystal approximant $\text{Al}_{13}\text{Os}_4$.** (a) Crystal structure of the decagonal approximant characterized with distorted pentagons and rhombi. The aperiodic layer at $\vec{b} = 0.0$ connects to the layer at $\vec{b} = 1/2$ to form an approximant decagonal structure. The red rhombus outlines the unit cell. (b) Periodic repetition of the unit cell along the \vec{b} direction, with a periodicity of 4.2 Å. (c) Two-dimensional quasi-periodic lattice in the ac -plane with a unit cell highlighted in red color. (d) Powder X-ray diffraction pattern (black markers) and Rietveld refinement (red line) of $\text{Al}_{13}\text{Os}_4$. (e) Temperature dependence of resistivity $\rho(T)$ at $H = 0$ T, showing the superconducting transition at $T_C = 5.47(2)$ K. (f) Temperature-dependent electronic specific heat (C_{el}), with the fitting of data using weak-coupling BCS model (solid black line). (g) Temperature-dependent ZFCW and FCC magnetization at an external field of 1.0 mT, demonstrating clear superconducting transition. (h) and (i) Temperature-dependent lower H_{C1} and upper H_{C2} critical fields, revealing the large upper critical field.

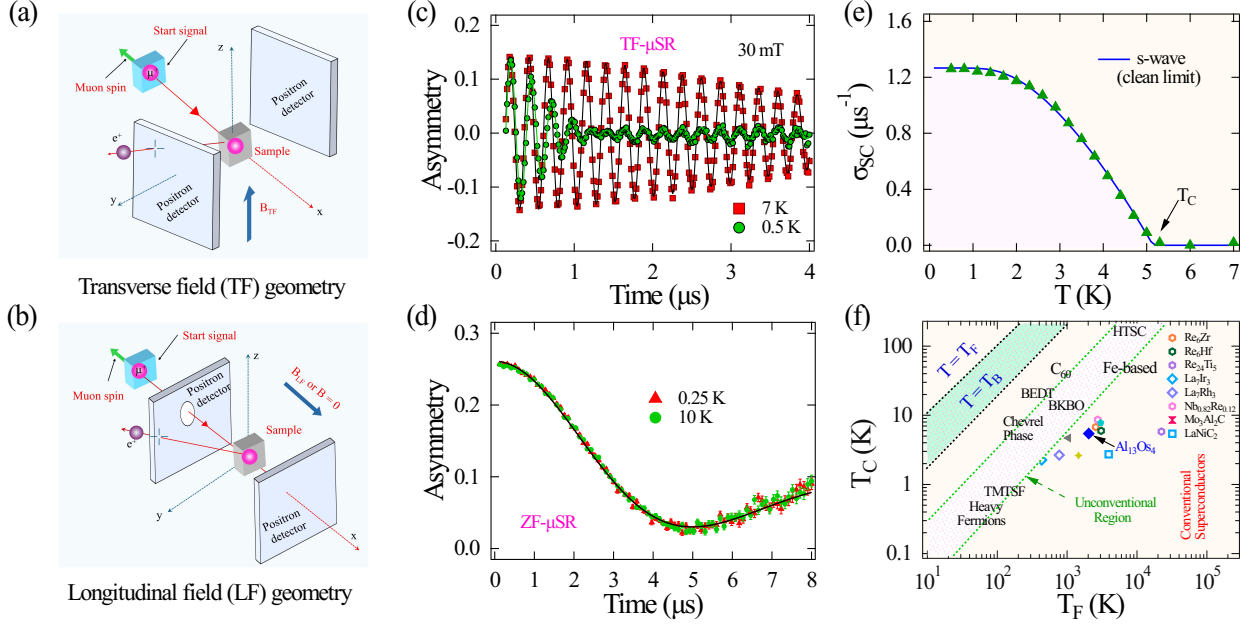


FIG. 2. Microscopic characterization of superconductivity in the decagonal quasicrystal approximant $\text{Al}_{13}\text{Os}_4$. Schematic diagram of the μSR set up for (a) transverse field (TF) and (b) longitudinal field (LF) configurations. Various directions are marked. (c) TF- μSR spectra obtained at 30 mT, both above and below superconducting T_C with relevant fits. (d) Zero field (ZF)- μSR spectra above and below T_C with a solid line fit representing the product of the static Kubo-Toyabe function and an exponential decay function. (e) Temperature-dependent superconducting relaxation rate (σ_{SC}) fitted with the isotropic conventional *s*-wave model. (f) Uemura plot between superconducting transition temperature T_C and Fermi temperature T_F for various types of superconductors.

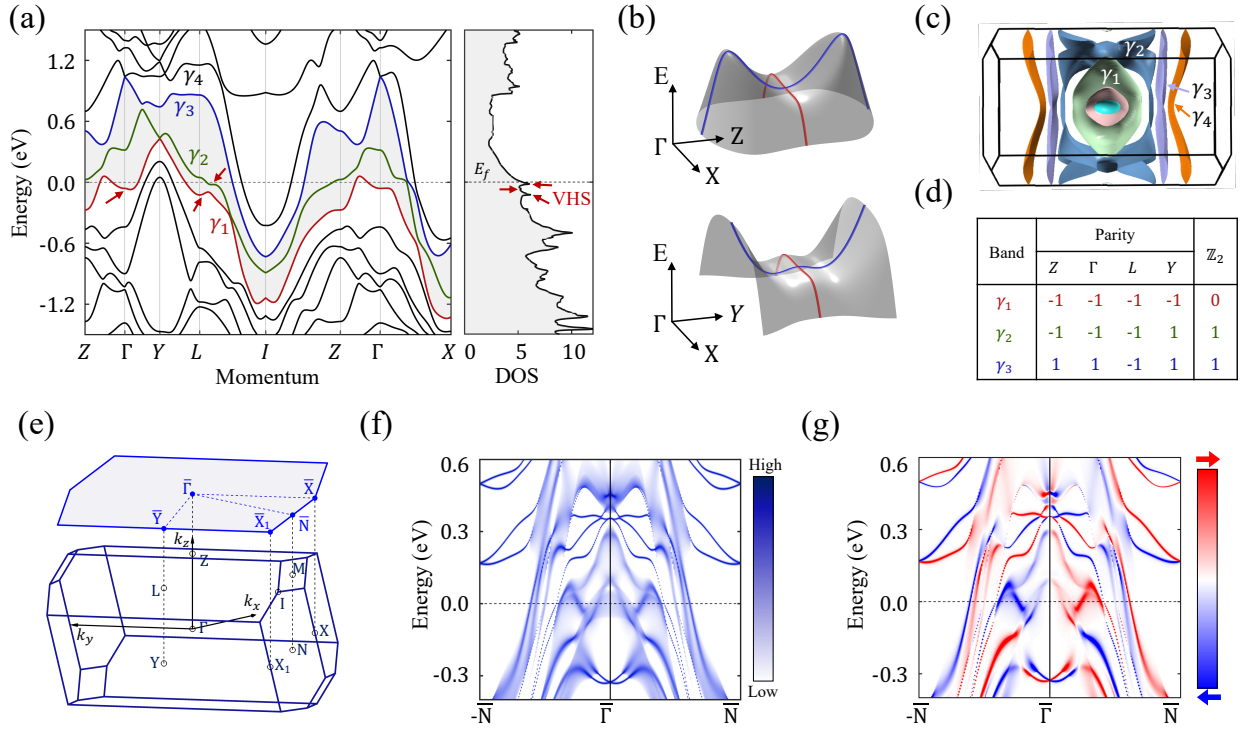


FIG. 3. **Nontrivial electronic topology of the decagonal quasicrystal approximant $\text{Al}_{13}\text{Os}_4$.**

(a) The band structure and density of states (DOS) incorporating spin-orbit coupling. The saddle-points van Hove singularities (vHSs) are indicated by red arrows. γ_1 , γ_2 , γ_3 , and γ_4 bands crossings the Fermi level are marked. The shaded gray color highlights a continuous band gap between various bands in the Brillouin zone (BZ). (b) Closeup of band structure around Γ resolving 3D saddle points with substantial flat band dispersion. (c) Fermi surface with various Fermi sheets in the BZ. (d) Parity and \mathbb{Z}_2 invariant of γ_1 , γ_2 , and γ_3 bands. (e) Bulk BZ and (001) surface projected BZ with various high-symmetry points. (f) (001) surface band structure and (g) associated spin-texture along $-\bar{N} - \bar{\Gamma} - \bar{N}$ direction. The spin-momentum-locked nontrivial surface states are observed within the projected bulk bandgap. Red and blue in (g) indicate up and down spin polarizations.